Mechanism of the growth pattern formation and three-dimensional morphological transition of hcp magnesium alloy dendrite

Jinglian Du,[1,2] Ang Zhang,[1,2] Zhipeng Guo,[1,2,*] Manhong Yang,[1,2] Mei Li,[3] and Shoumei Xiong[1,2,*]

[1]*School of Materials Science and Engineering, Tsinghua University, Beijing 100084, China*

[2]*Laboratory for Advanced Materials Processing Technology, Ministry of Education, Tsinghua University, Beijing 100084, China*

[3]*Materials Research Department, Research and Innovation Center, Ford Motor Company, MD3182, P.O. Box 2053, Dearborn, Michigan 48121, USA*

(Received 9 April 2018; published 3 August 2018)

Based on an anisotropy function with the anisotropic strength determined via atomistic calculations, the mechanism of the three-dimensional (3D) growth pattern formation of magnesium alloy dendrite is investigated by performing phase-field simulations with the parallel adaptive-mesh-refinement algorithm. It is found that the 3D morphological transition of the α-Mg dendrite is dependent on the growth parameters, including the partition coefficient, the anisotropic strength, and the supercooling during solidification. The α-Mg dendrite exhibits growth tendency along both the basal and nonbasal directions, but the dendritic growth tendency along the basal direction is weaker. Consequently, the 3D morphology of the α-Mg dendrite would transform from an 18-primary-branch pattern to a 12-primary-branch pattern if the local growth driving force on the basal plane is insufficient. During dendrite growth, the solute concentration increases as the distance from the dendritic nucleus center increases, and reaches the local maximum at the solid/liquid interface, beyond which it decreases before reaching a constant value. The simulation results agree well with those found in experiments and the existing solidification theory.

DOI: 10.1103/PhysRevMaterials.2.083402

I. INTRODUCTION

Magnesium alloys have attracted considerable scientific and technological interests because they are promising candidates for lightweight materials used in automobile, airplane, and biomedical fields, etc. [1–7]. The α-Mg dendrite constitutes the primary phase of Mg-based alloys, and thus the dendritic orientation, distribution, and morphological preference have significant influences on the practical performance of the alloys [8–11]. The existence of surface anisotropy drives the α-Mg dendrite to grow along certain crystallographic orientations, leading to diverse growth patterns with complicated dendritic morphology in three dimensions [12–14]. This is especially true for the Mg-based alloys with hexagonal lattice structure, comparing with their counterparts with cubic lattice structure like nickel-based alloys [15–21].

By the numerical simulation, it was found that the α-Mg dendrite presents a platelike shape in 3D, which is induced by a slower growth along $\langle 0001\rangle$ and a faster growth along $\langle 11\bar{2}0\rangle$ [22,23]. Through the metallography and electron backscattered patterns (EBSP) techniques, it was shown that the α-Mg dendrite grows along $\langle 11\bar{2}0\rangle$ and $\langle 22\bar{4}5\rangle$ with six and three secondary arms, respectively [24,25]. Based on the synchrotron x-ray tomography and electron backscattered diffraction (EBSD) experiments, it was confirmed that the α-Mg dendrite grows along six $\langle 11\bar{2}0\rangle$ basal directions and twelve $\langle 11\bar{2}x\rangle$ nonbasal directions, resulting in an 18-primary-branch pattern in 3D [9,26]. In addition, a dendritic morphological transformation from 18-primary branches to 12-primary branches [27], i.e., dendrite orientation transition (DOT), is observed for the α-Mg dendrite. The microstructure of the α-Mg dendrite is also found to be affected by the solute concentration, resulting in both dendritic and seaweed type grains [10,13]. Subsequently, relevant atomistic simulations based on the density functional theory (DFT) further confirm the complex growth behavior of the hexagonal-close-packed (hcp) α-Mg dendrite [28,29].

Research revealed that the growth pattern formation of the dendritic microstructure is associated with various factors, including the growth parameters, the anisotropy of materials properties, and the additional elements, etc. [10,27,30,31]. To date, most research is largely focused on a qualitative level or at least a semiquantitative level, and the underlying mechanism of the 3D dendritic morphological formation in relation to the dendritic growth orientation of the magnesium alloy is still unclear or not completely understood. Therefore, investigation on the 3D growth pattern formation of the hcp α-Mg dendrite at atomic level is necessary for understanding the dendritic microstructure evolution during solidification, thus providing theoretical guidance for improving the mechanical properties and practical performances of magnesium alloys.

In this work, the underlying mechanism of the growth behavior of magnesium alloy dendrite and the effects of growth parameters on dendritic morphological transition is investigated by performing 3D phase-field simulations. An anisotropy function developed on the basis of hexagonal structure symmetry and experimental findings, is coupled into the phase-field model to simulate the 3D morphological evolution of the hcp α-Mg dendrite [30,32–34]. The anisotropic strength is determined quantitatively via the DFT-based atomistic

*Corresponding authors: zhipeng_guo@mail.tsinghua.edu.cn; smxiong@tsinghua.edu.cn

calculations on the anisotropic surface energy of different crystallographic directions. The results show that the hcp α-Mg dendrite exhibits potential growth tendency along different directions, but the dendrite growth tendency along the basal directions is weaker than that along the nonbasal directions. In addition, it is found that the growth parameters such as the partition coefficient, the anisotropic strength, and the supercooling conditions are responsible for the dendritic morphological transition, and could alter the dendritic pattern formation of magnesium alloy significantly.

II. MODEL AND METHODOLOGY

A. Atomistic simulation scheme

The atomic structure of binary Mg-based alloys is constructed using the solid solution model, with the crystallographic information of Mg referred from a Pearson handbook [35–37]. The atomic configuration for anisotropic surface energy calculation is simulated by the slab model [38,39]. Accordingly, different surface slab models corresponding to those surface orientations associated with the preferred growth directions of the hcp α-Mg dendrite are obtained. All of the DFT-based atomistic simulations are performed via the Vienna Ab initio Simulation Package (VASP) [40,41]. The exchange and correlation interaction is described by the local density approximation (LDA) [42]. The interaction between ions and valence electrons is modeled by the projector-augmented-wave (PAW) potentials [43]. A plane-wave cutoff energy of 420 eV is used in the calculation. Brillouin zone integration is modeled by the Monkhorst-Pack k-point mesh, and the k-point separation in the Brillouin zone of the reciprocal space is set as $0.01\,\text{Å}^{-1}$ for each unit cell. Relevant numerical tests are performed to ensure the convergence and accuracy of the computational scheme. The total energy is converged to $5 \times 10^{-7}\,\text{eV/atom}$ with respect to electronic, ionic, and unit cell degrees of freedom.

The anisotropic surface energy ($\gamma_{\{hkil\}}$) is used to quantify the anisotropic strength along different directions by using a least-square regression method [29,44,45]. For a certain crystallographic plane $\{hkil\}$, the anisotropic surface energy $\gamma_{\{hkil\}}$ can be obtained via

$$\gamma_{\{hkil\}} = \frac{E^n_{\text{slab}} - nE_{\text{bulk}}}{2S}, \tag{1}$$

where E^n_{slab} is the total energy per primitive slab unit cell, n is the layer number of the surface slab model, E_{bulk} is the total energy per primitive bulk unit cell, S is the surface area per primitive slab unit cell, and the factor of 2 accounts for two equivalent surfaces of a particular slab model. The calculated anisotropic surface energy is satisfactorily converged to $<0.001\,\text{eV/Å}^2$ with respect to the slab thickness, the relaxed atomic layers, and the vacuum thickness. Details on the surface energy calculation and the anisotropic strength determination have been reported elsewhere [12,29], and no further illustration would be given here.

B. Anisotropy function model

The growth behavior of the magnesium alloy dendrite with an hcp lattice structure is significantly different from that with an face-centered-cubic (fcc) or body-centered-cubic (bcc) lattice structure. In solidification numerical modeling, a feasible expression of surface anisotropy function is essential for an accessible prediction of dendritic microstructure. For the hcp α-Mg dendrite, a general anisotropy function developed in literature [16,46] is

$$d_{\text{hex}}(\vec{n}) = 1 + \delta_{\text{hex}}\left(n_x^6 - 15n_x^4n_y^2 + 15n_x^2n_y^4 - n_y^6 + 5n_z^4 - 5n_z^2 + 6n_z^6\right), \tag{2}$$

where δ_{hex} is the anisotropy coefficient, and $\vec{n}$ is the unit vector normal to the solid/liquid interface. This model could describe the sixfold symmetrical growth pattern of the α-Mg dendrite in the basal plane and the dendritic growth along the principal direction (i.e., $\langle 0001\rangle$), but the simulated 3D growth pattern deviates significantly from the practical dendritic morphology observed in experiments [10,22,23]. To further investigate the growth behavior of the hcp α-Mg dendrite, an anisotropy function is developed by combining certain terms of spherical harmonics based on the hcp structure symmetry and the experimental findings [9,29]. The resultant formulation of the anisotropy function model is expressed as

$$A(\vec{n}) = \gamma_0 \cdot \left\{1 + \varepsilon_1 \cdot \left(3n_z^2 - 1\right)^2 + \varepsilon_2 \cdot \left(n_x^3 - 3n_x \cdot {n_y}^2\right)^2 \times \left[9n_z^2 - (1 + \varepsilon_3)\right]^2\right\}, \tag{3}$$

where ε_i ($i = 1, 2,$ and 3) are the anisotropic strength for describing the dendritic growth tendency along different crystallographic directions. In particular, ε_1 is associated with the dendritic growth along $\langle 0001\rangle$, whereas ε_2 and ε_3 are associated with $\langle 11\bar{2}0\rangle$ and $\langle 11\bar{2}x\rangle$. ε_1, ε_2, and ε_3 are determined from the anisotropic surface energy obtained via the DFT-based calculations [29], results of which are listed in Table I.

TABLE I. The anisotropic strength $\varepsilon_i (i = 1, 2,$ and 3) of the hcp α-Mg dendrite estimated by relevant DFT-based calculations.

Anisotropic strength $\varepsilon_i (i = 1, 2,$ and 3)	Lower value	Upper value
ε_1	−0.0629	−0.0317
ε_2	0.0422	0.1344
ε_3	−0.5843	0.0594

C. Phase-field modeling scheme

The phase-field model developed by Echebarria *et al.* [47] is employed here to simulate the dendritic microstructure evolution of magnesium alloys during solidification. In particular, the phase-field variable $\phi(\vec{x}, t)$ is adopted to describe the distribution of different phases, i.e., $\phi = 1$ denotes the primary α phase, $\phi = -1$ denotes the liquid phase, while $-1 < \phi < 1$ denotes the solid/liquid interface region [32]. The governing

equations are expressed as

$$\tau\frac{\partial\phi}{\partial t}=\nabla\cdot[W(\vec{n})^2\nabla\phi]+\frac{\partial}{\partial x}\left(|\nabla\phi|^2W(\vec{n})\frac{\partial W(\vec{n})}{\partial\phi_x}\right)+\frac{\partial}{\partial y}\left(|\nabla\phi|^2W(\vec{n})\frac{\partial W(\vec{n})}{\partial\phi_y}\right)+\frac{\partial}{\partial z}\left(|\nabla\phi|^2W(\vec{n})\frac{\partial W(\vec{n})}{\partial\phi_z}\right)+\phi(1-\phi^2)-\lambda(1-\phi^2)^2(\theta+kU), \quad (4)$$

$$\left(\frac{1+k}{2}-\frac{1-k}{2}\phi\right)\frac{\partial U}{\partial t}=\nabla\cdot\left(D\frac{1-\phi}{2}\nabla U-\vec{j}_{\rm at}\right)+\frac{1}{2}[1+(1-k)U]\frac{\partial\phi}{\partial t}, \quad (5)$$

$$\frac{\partial\theta}{\partial t}=\alpha\nabla^2\theta+\frac{1}{2}\frac{L/c_p}{\Delta T_0}\frac{\partial\phi}{\partial t}, \quad (6)$$

where τ is the relaxation time, $W(\vec{n})$ is the anisotropic width of the diffuse interface, $\vec{n}$ is the unit normal vector of the solid/liquid interface, k is the partition coefficient, D and α are the solute and thermal diffusivities, respectively, L is the heat of fusion per unit volume, c_p is the specific heat, $\phi_x=\partial\phi/\partial x$, $\phi_y=\partial\phi/\partial y$, and $\phi_z=\partial\phi/\partial z$. λ is the scaled parameter with its reciprocal measuring the height of the dimensionless energy barrier of the double-well potential (H), which is given as

$$\lambda=\frac{15}{16}\frac{RT_M(1-k)}{v_0H|m|}\Delta T_0, \quad (7)$$

where R is the gas constant, T_M is the melting temperature, v_0 is the molar volume, and m is the liquidus slope in the phase diagram. θ is the dimensionless temperature and denoted as

$$\theta=\frac{T-T_M-mc_\infty}{\Delta T_0}. \quad (8)$$

U is the dimensionless solute concentration and given as

$$U=\frac{\frac{2c/c_\infty}{1+k-(1-k)\phi}-1}{1-k}, \quad (9)$$

where c is the solute concentration and c_∞ is the initial solute concentration. $\vec{j}_{\rm at}$ is the "antitrapping" current defined as

$$\vec{j}_{\rm at}=-\frac{W}{\sqrt{2}}\frac{c/c_\infty}{[1+k-(1-k)\phi]}\frac{\partial\phi}{\partial t}\frac{\nabla\phi}{|\nabla\phi|}. \quad (10)$$

ΔT_0 is the equilibrium freezing temperature range related to c_∞ and denoted as

$$\Delta T_0=\frac{|m|c_\infty(1-k)}{k}. \quad (11)$$

The anisotropy function $A(\vec{n})$ is incorporated by $\tau=\tau_0A(\vec{n})^2$ and $W(\vec{n})=W_0A(\vec{n})$. The kinetic effect can be ignored by taking

$$\tau=\tau_0\{k[1+(1-k)U]\}A(\vec{n})^2. \quad (12)$$

To avoid the selection of physical parameters, the dimensionless form of the length and the time is scaled by the diffuse interface width and the relaxation time:

$$W_0=\frac{\lambda d_0}{a_1},\quad \tau_0=\frac{d_0^2a_2\lambda^3}{Da_1^2}, \quad (13)$$

where $a_1=0.8839$ and $a_2=0.6267$ are the constants, while d_0 is the chemical capillary length and denoted as

$$d_0=\frac{\Gamma}{\Delta T_0}, \quad (14)$$

where Γ is the Gibbs-Thomson coefficient. It is worth stressing that during solidification, both the surface energy anisotropy and the kinetic anisotropy play important roles in determining the microstructure formation [48–52]. However, in most common solidification conditions, the dendritic growth is driven by the solute diffusion, during which case the dendritic growth direction and pattern formation are primarily determined by the thermodynamic effect related surface energy anisotropy in light of the underlying lattice structure [14,46,53]. During the rapid solidification with large supercooling conditions, the microstructure formation is mainly associated with the kinetic anisotropy forming in a way of solute trapping and the local solute redistributions near the solid/liquid interface [54,55]. In this respect, the dendritic growth pattern and orientation selection during common solidification is mostly determined by the thermodynamic effect related surface energy anisotropy instead of the kinetic anisotropy, which is not considered in the solidification dominated by the solute diffusive effect.

The phase-field equations are solved via the parallel adaptive-mesh-refinement (Para-AMR) algorithm developed by the current authors [30,32]. It has been demonstrated that such Para-AMR algorithm could enhance the computational efficiency significantly by two to three orders of magnitude [33,56]. The anisotropy function with the anisotropic strength determined from DFT-based calculations, i.e., Eq. (3), is incorporated into the phase-field model to simulate the α-Mg dendrite growth. The 3D phase-field simulations are performed using the hierarchical mesh with five levels of grids. The dendritic seeds are planted in the liquid alloy at the center of the simulation domain with an initial radius of $3.2W_0$. The 3D computing domain is equivalent to $1024\times1024\times1024$ meshes on the finest grid level, i.e., $dx=dy=dz=0.8$. The scaled parameter is chosen to be $\lambda=30$. Detailed growth parameters of different simulation cases are listed in Table II.

D. Model validation

For the simulation of dendritic microstructure, the grids at the solid/liquid interface need to be refined in light of the AMR algorithm, because the variables change the fastest and the gradient reaches the maximum value at this region. On each grid level, a cluster algorithm is adopted to separate the tagged grids into the patch boxes (i.e., clusters filled by meshes). The algorithm is achieved firstly by tagging the cells based on the gradient criterion defined as

$$|\nabla\phi|+\beta_U|\nabla U|+\beta_\theta|\nabla\theta|\geqslant\xi, \quad (15)$$

where ξ is a threshold value retrieved from relevant numerical tests, while β_U and β_θ are the weight coefficients of solute and temperature, respectively. The structure of the patch boxes on

TABLE II. The growth parameters of the α-Mg dendrite, including the partition coefficient (k), the anisotropic strength (ε_i, i = 1, 2, and 3) along different directions, and the supercooling (u) during solidification.

		Growth parameters				
Group No.	Case No.	k	u	ε_1	ε_2	ε_3
I	1	0.13	0.10	−0.050	0.074	−0.077
	2	0.15	0.10	−0.050	0.074	−0.077
	3	0.24	0.10	−0.050	0.074	−0.077
	4	0.29	0.10	−0.050	0.074	−0.077
	5	0.30	0.10	−0.050	0.074	−0.077
	6	0.31	0.10	−0.050	0.074	−0.077
	7	0.32	0.10	−0.050	0.074	−0.077
II	1	0.37	0.12	−0.050	0.080	0.059
	2	0.37	0.13	−0.050	0.080	0.059
	3	0.37	0.14	−0.050	0.080	0.059
	4	0.37	0.15	−0.050	0.080	0.059
	5	0.37	0.17	−0.050	0.080	0.059
	6	0.37	0.20	−0.050	0.080	0.059
	7	0.37	0.22	−0.050	0.080	0.059
III	1	0.135	0.10	−0.050	0.080	0.059
	2	0.135	0.10	−0.050	0.080	−0.035
	3	0.135	0.10	−0.050	0.080	−0.169
	4	0.135	0.10	−0.050	0.080	−0.463
	5	0.135	0.10	−0.050	0.040	−0.463
	6	0.135	0.10	−0.050	0.040	0.059
	7	0.135	0.10	−0.050	0.130	−0.463
	8	0.135	0.10	−0.050	0.130	0.059

every grid level is properly nested. The finer grids are contained inside the coarser grids. All of the grids comprise a hierarchical architecture with different patch boxes setting at each grid level after AMR.

The according grid structure and mesh architecture of the patch boxes during AMR of a typical hcp α-Mg dendrite is illustrated in Fig. 1. The variation of the local box density demonstrates that the mesh refinement accommodates well with the refinement of the solid/liquid interface, as shown in Figs. 1(a) and 1(b), respectively. Meanwhile, the physical properties of materials are assumed to be constants and the solute diffusion in solid phase is neglected during simulation. The

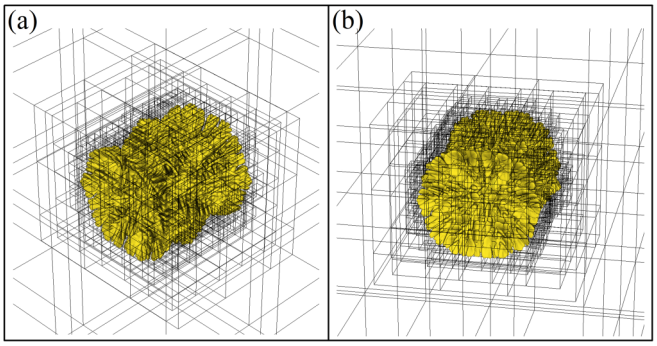

FIG. 1. Hierarchical mesh architecture of the patch boxes during the AMR of the hcp α-Mg dendrite. (a) and (b) show the perspective viewed along ⟨111⟩ and ⟨125⟩, respectively.

periodic boundary conditions are adopted for the phase field and solute field, whereas the isothermal conditions are considered for the temperature. As the dendrite growth proceeds, the computing time per time step increases because the net grid number, particularly at the top level, increases considerably as the solid/liquid interface region increases during solidification. Numerical tests with respect to the accuracy and efficiency of the Para-AMR algorithm have been performed and reported in our previous work [30,32,56,57].

III. RESULTS AND DISCUSSION

A. Typical dendritic growth pattern

Figure 2(a) shows the typical growth pattern of the simulated hcp α-Mg dendrite. The coordination system is depicted at the bottom right corner, where the z axis is along the principal direction (i.e., ⟨0001⟩), and the x-y plane corresponds to the basal plane. As shown, the hcp α-Mg dendrite presents a sixfold symmetrical pattern viewed along the z axis, and there are three layers with each having six-primary branches viewed along the x and/or y axis. Consequently, the dendritic morphology exhibits an 18-primary-branch pattern in 3D. These 18-primary branches growing out from the seed center could be further classified into two categories: one is the 6-primary branches along the basal directions, and the other is the 12-primary branches along nonbasal directions. The secondary arms of the hcp α-Mg dendrite exhibit the same growth direction as the primary dendritic stem direction. This is significantly different from a typical fcc α-Al dendrite, which normally exhibits a fourfold symmetrical pattern in two dimensions and the dendritic morphology presents six primary branches in three dimensions, as shown in Fig. 2(b). In addition, the 6-primary branches growing out from the dendritic nucleus center gradually evolve into a paraboloid shape connected by four fin-shape-like subarms. These distinctions in dendritic morphology between the hcp α-Mg dendrite and the fcc α-Al dendrite primarily originate from the intrinsic difference of the underlying lattice structure and the according surface energy anisotropy [26,29].

B. Influence of partition coefficient (k)

The partition coefficient (k) is the ratio between the solute concentration in the solid phase (C_s) and that in the liquid phase (C_l) at a given temperature, i.e., $k = C_s/C_l$ [58–60]. Once nucleation occurs, the subsequent growth of the solid phase is controlled by the diffusion of solute atoms. For dendritic microstructure, the solute diffusion rate in the liquid phase is significantly larger than that in the solid phase [19]. In the practical situation, the magnitude of k is generally not constant and depends on the local concentration. Accordingly, the influence of the partition coefficient on the growth pattern of the hcp α-Mg dendrite is investigated with parameters listed in Table II designated as group I. Attention is focused on the cases when $k < 1$, where the solute solubility in the solid phase is less than that in the liquid phase.

Figures 3(a_1)–3(h_1) show the simulated 3D dendritic morphology when $k = 0.12$, 0.13, 0.15, 0.18, 0.21, 0.24, 0.28, and 0.31, respectively. To achieve a better understanding on the 3D growth pattern of the hcp α-Mg dendrite,

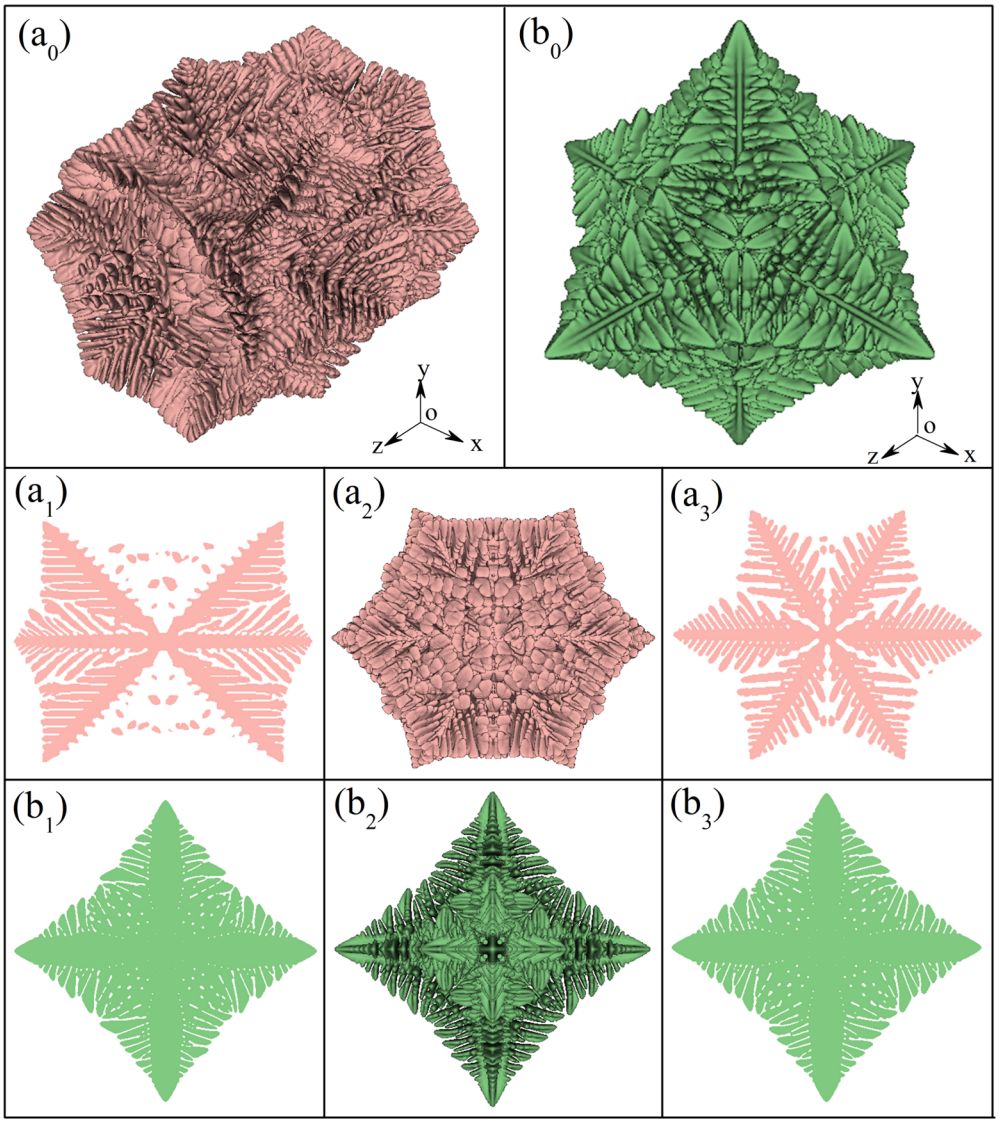

FIG. 2. Growth pattern of a typical simulated dendrite with (a) hcp lattice structure, e.g., the α-Mg dendrite and (b) fcc lattice structure, e.g., the α-Al dendrite. (a_0), (a_2) and (b_0), (b_2) show the 3D morphology viewed from $\langle 111 \rangle$ and $\langle 001 \rangle$. The according 2D sections cut by $\{010\}$ and $\{001\}$ sections are shown in (a_1), (a_3) and (b_1), (b_3), respectively.

the two-dimensional (2D) projections viewed from the $\langle 11\bar{2}0 \rangle$ and $\langle 0001 \rangle$ are presented in Figs. 3(a_2)–3(h_2) and 3(a_3)–3(h_3), respectively. In addition, the 2D sections cut by the $\{10\bar{1}0\}$ and $\{0001\}$ planes are presented in Figs. 3(a_4)–3(h_4) and 3(a_5)–3(h_5). The results show that the hcp α-Mg dendrite grow faster when k is lower, as indicated by the size of the primary and secondary dendrite arms. As k increases, the 3D dendritic morphology transforms from an 18-primary-branch pattern to a 12-primary-branch pattern. The fact that the 6-primary branches of the hcp α-Mg dendrite along the basal direction ceased to grow agrees well with the DOT phenomenon observed in experiments [26,27]. This indicates that the dendritic growth tendency along the nonbasal directions is larger than that along the basal ones, as is also reflected by the magnitude of the crystallographic anisotropy [26,29]. In this respect, the dendritic growth tendency along the basal directions could be inhibited when the hcp α-Mg dendrite does not have enough driving force to grow, such as the case when k is larger [46,61,62]. As shown in Fig. 3, a higher solute concentration or partition coefficient leads to a lower growth velocity and thus shorter dendritic primary branches and/or secondary arms.

Figure 4 shows the variation of the solute concentration when $k = 0.31$ at the time step of 8000, 28 000, 52 000, 76 000, and 100 000, respectively. The results indicate that as the solidification proceeds, the solute concentration in the liquid phase increases, and such increase of solute concentration continues until a steady growing state is achieved. On the other hand, the solute concentration in the solid phase increases slightly from its original state to an equilibrium value. As shown in Fig. 4(a), the solute concentration increases as the distance from the dendritic nucleus center increases and achieves a local maximum at the solid/liquid interface, after which it decreases before reaching a constant value. The inset of Fig. 4(b) is a zoomed-in area of the solute concentration at the time step of 52 000. It is found that as the dendrite

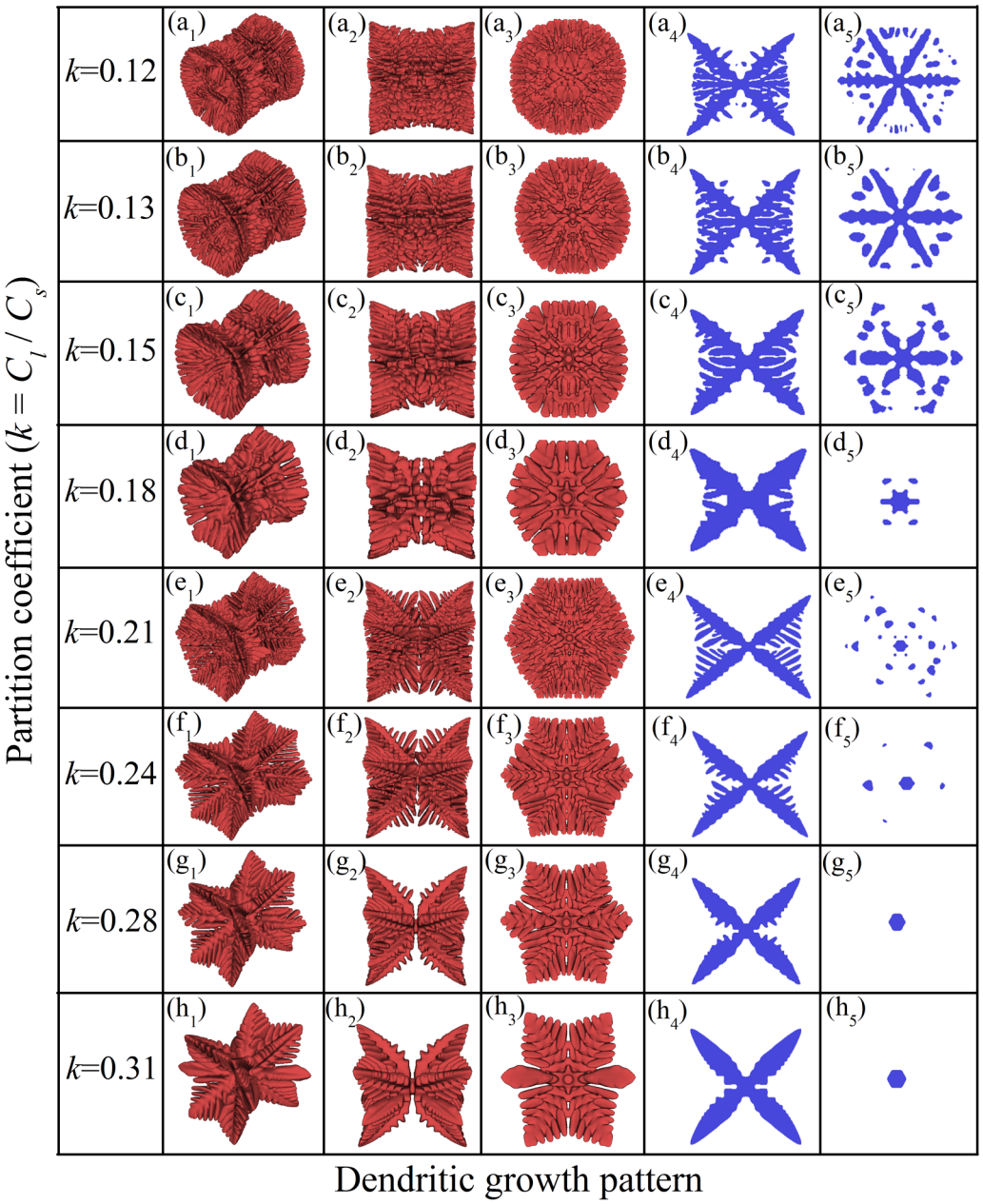

FIG. 3. Growth pattern and morphological transition of the hcp α-Mg dendrite with different solute partition coefficient (k). The 3D dendritic morphology is shown in the second column. The 2D projections viewed along $\langle 11\bar{2}0\rangle$ and $\langle 0001\rangle$ are shown in the third and fourth columns, respectively. The 2D sections cut by the $\{10\bar{1}0\}$ and $\{0001\}$ sections are shown in the fifth and sixth columns, respectively.

grows further, the solute concentration difference at the front of the solid/liquid interface become less significant, and thus the solute concentration in the liquid phase distributes more uniformly than that at the initial growth stage, indicating that the growth rate of the hcp α-Mg dendrite become slower with the solidification proceeding.

The evolution of the 3D growth pattern for the hcp α-Mg dendrite at different times when $k = 0.31$ is shown in Fig. 5. The coordination system is depicted at the lower right corner in each subfigure, where the z axis is along the principal direction (i.e., $\langle 0001\rangle$). Figure 5(a) shows the 3D dendritic morphology at the initial growing stage of the hcp α-Mg dendrite; it can be observed clearly that there are two layers with each layer having six-primary branches viewed along the x and/or y axis, but no primary branches are observed along the z axis. Accordingly, the resultant 3D dendritic morphology exhibits a 12-primary-branch pattern, and the secondary dendritic arms grow along the same direction as that of the primary branches, as shown in Figs. 5(b)–5(i).

Figure 6 shows the solute concentration variation versus the distance from the solid/liquid interface at the time step of 52 000. The corresponding correlation between the partition coefficient and the maximum solute concentration (i.e., the value at the solid/liquid interface) is presented in the inset. The results indicated that the solute concentration in the liquid changes exponentially, and such variation is associated with

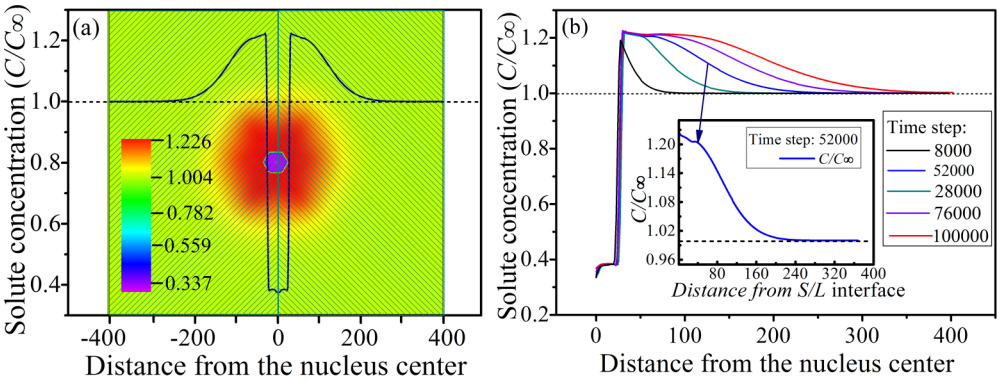

FIG. 4. (a) Solute concentration distribution at the time step of 52 000, and (b) solute concentration variation with the distance from the dendritic nucleus center at different time steps during dendrite growth with $k = 0.31$.

the growth rate and solute diffusion coefficient. Furthermore, the solute concentration decreases as the distance from the solid/liquid interface increases and it varies slightly slower when the partition coefficient is lower. This behavior is in qualitative agreement with previous solidification theory and experimental results [60,63,64]. In addition, the maximum solute concentration decreases as the partition coefficient increases. When the partition coefficient is lower, more solute atoms are accumulated at the solid/liquid interface, leading to a more inhomogeneous distribution.

C. Influence of anisotropic strength (ε)

The surface anisotropy plays an important role in the selection of the operating state during dendrite growth [19,65]. The dendritic microstructure formation is associated with the

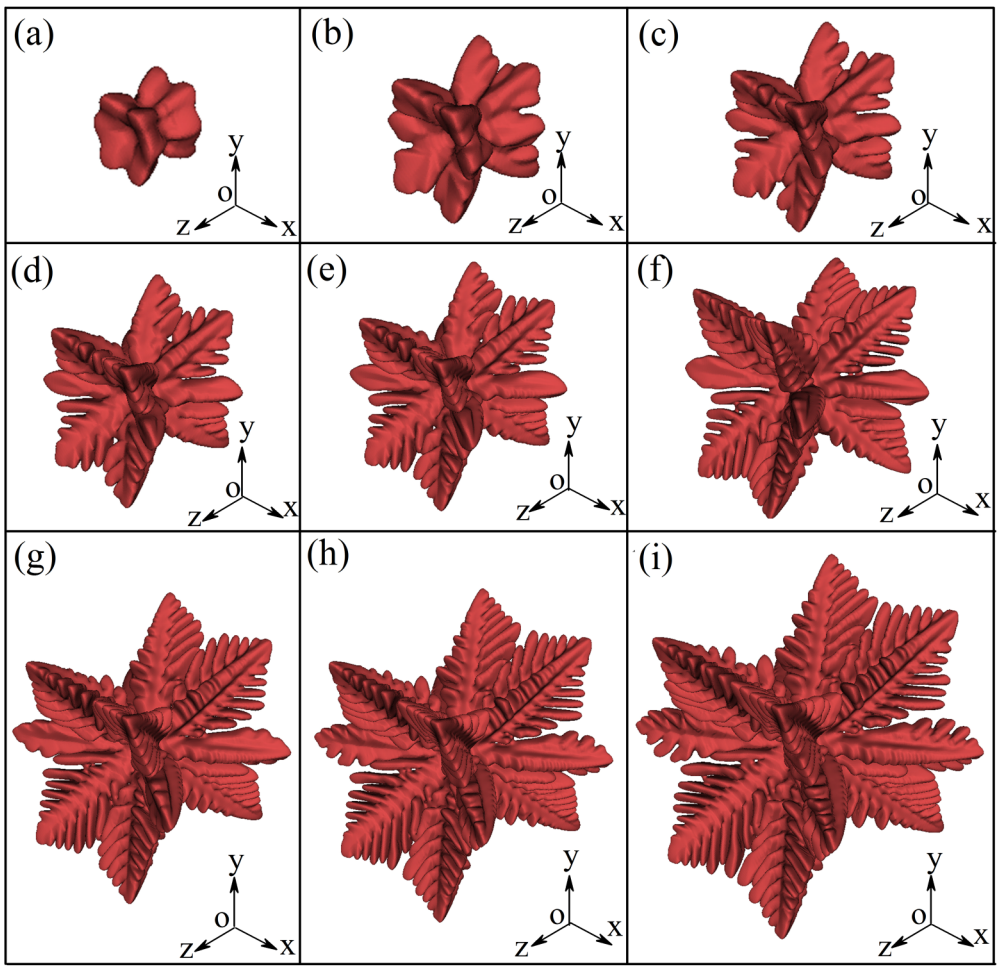

FIG. 5. Phase-field simulation on the hcp α-Mg dendrite growth pattern with 12-primary branches at the different time steps of (a) 8000, (b) 16 000, (c) 24 000, (d) 32 000, (e) 40 000, (f) 48 000, (g) 56 000, (h) 64 000, and (i) 72 000, respectively.

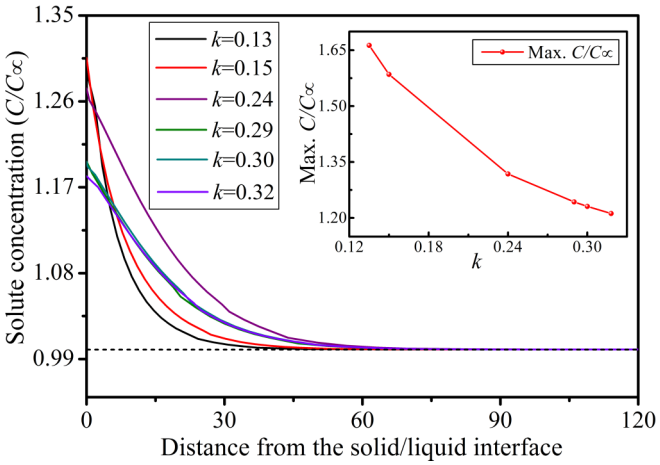

FIG. 6. Solute concentration (C/C_∞) distribution in the liquid region at the front of the solid/liquid interface under different partition coefficient (k). The inset shows the according correlation between the partition coefficient (k) and the solute concentration at the solid/liquid interface (i.e., the maximum solute concentration).

magnitude of anisotropic strength along different crystallographic directions [14,66]. Accordingly, phase-field simulations (i.e., group III in Table II) are performed to investigate the influence of anisotropic strength (ε_i, $i = 1, 2, 3$) on the growth pattern formation of the hcp α-Mg dendrite. Because no growth tendency along the principal direction (i.e., $\langle 0001 \rangle$) is observed in experiments [12,26], the simulations are performed by fixing $\varepsilon_1 = -0.050$, whereas changing ε_2 and ε_3. It is worth stressing that the anisotropic strength is determined quantitatively by performing relevant DFT-based atomistic calculations [29], the results of which are listed in Tables I and II.

Figures 7(a_1)–7(d_1) show the simulated 3D morphology of the hcp α-Mg dendrite when $\varepsilon_2 = 0.080$ and $\varepsilon_3 = -0.463$, -0.169, -0.035, and 0.059, respectively. Figures 7(a_2)–7(d_2) and 7(a_3)–7(d_3) show the according 2D projections of the hcp α-Mg dendrite viewed from $\langle 11\bar{2}0 \rangle$ and $\langle 0001 \rangle$, respectively. The corresponding 2D sections of the $\{10\bar{1}0\}$ and $\{0001\}$ planes are shown in Figs. 7(a_4)–7(d_4) and 7(a_5)–7(d_5), respectively. The results indicate that as ε_3 increases from -0.463 to 0.059, the 3D dendritic morphology transforms from a 12-primary-branch pattern to an 18-primary-branch pattern, i.e., the six primary branches on the basal plane exhibit at a larger ε_3. Figures 7(e_1)–7(h_1) show the simulated 3D morphology of the hcp α-Mg dendrite with different combinations of ε_2 and ε_3. The third and fourth columns show the 2D projections viewed from $\langle 11\bar{2}0 \rangle$ and $\langle 0001 \rangle$, whereas the 2D projections on the $\{10\bar{1}0\}$ and $\{0001\}$ planes are presented in the fifth and sixth columns, respectively. It is found that the dendritic morphological transition also occurs by increasing ε_2 from 0.040 to 0.130 with a fixed $\varepsilon_3 = 0.059$, as shown in Figs. 7(g), 7(d), and 7(h), respectively. By fixing ε_3 at -0.0463, the hcp α-Mg dendrite exhibits a 12-primary-branch pattern regardless of ε_2, as shown in Figs. 7(a), 7(e), and 7(f).

In this respect, the growth tendency of the hcp α-Mg dendrite along the six basal directions is inhibited when ε_3 is negative, resulting in a 12-primary-branch pattern in 3D. On the other hand, a positive ε_3 tends to promote the hcp α-Mg dendrite growth along the basal directions, inducing an 18-primary-branch pattern, as shown in Figs. 7(a), 7(e), and 7(f), together with Figs. 7(d), 7(g), and 7(h). Figures 8(a) and 8(b) show the solute concentration variation with the distance from the solid/liquid interface corresponding to different ε_3 at the time steps of 8000 and 24 000, respectively. The inset shows the according correlation between ε_3 and the solute concentration at the solid/liquid interface (i.e., the maximum value of solute concentration). The results indicate that an increase of ε_3 could widen the difference of the solute concentration. Therefore, the 3D growth pattern formation of the hcp α-Mg dendrite is determined by the combined effect of the anisotropic strength ε_2 and ε_3, which controls the dendrite growth along both the basal and nonbasal directions.

D. Influence of supercooling ($u = -\theta$)

As the driving force for crystal nucleation and growth, supercooling is an important parameter related to dendritic microstructure formation and dendritic morphological evolution during solidification [10,12,66]. In this respect, different simulations (i.e., group II in Table II) are performed to investigate the effect of supercooling on the growth pattern formation of hcp α-Mg dendrite. Figures 9(a_1)–9(g_1) show the simulated results of the dendritic growth pattern under different undercooling conditions, i.e., $u = 0.12$, 0.13, 0.14, 0.15, 0.17, 0.20, and 0.22, respectively. To further understand the complex dendritic morphology, the α-Mg dendrite is cut by using different crystallographic planes. Figures 9(a_2)–9(g_2) and 9(a_3)–9(g_3) show the according 2D projections of the hcp α-Mg dendrite viewed from $\langle 11\bar{2}0 \rangle$ and $\langle 0001 \rangle$, respectively. Whereas, the 2D projections cut by the $\{10\bar{1}0\}$ and $\{0001\}$ planes are shown in Figs. 9(a_4)–9(g_4) and 9(a_5)–9(g_5), respectively.

It is found that the hcp α-Mg dendrite grows faster under a larger supercooling condition, which could also be reflected by both the size and the intensity of the dendritic primary and secondary arms. As shown in Figs. 9(a_5)–9(g_5), the hcp α-Mg dendrite exhibits a 12-primary-branch pattern under lower undercooling conditions, whereas the six-primary branches along the basal directions exhibits when the supercooling is larger. This simulated result agrees well with the DOT phenomenon observed in experiment [26,27]. It is found that the hcp α-Mg dendrite exhibits potential growth tendency along the six basal directions under both high and low supercooling conditions, which agrees with the results predicted from DFT-based calculations [12,26]. The difference is that the dendritic growth tendency along the nonbasal directions is larger than that along the basal directions, as reflected by the distinctions of the surface energy anisotropy [26,29]. In this respect, the hcp α-Mg dendrite growth along the six basal directions could be inhibited under the small supercooling conditions.

Figure 10 shows the 3D morphological evolution of the hcp α-Mg dendrite at different time steps when $u = 0.20$. The coordinate system is also depicted at the bottom right corner of each subfigure. Figure 10(a) shows the 3D growth pattern of an α-Mg dendrite at the initial solidification stage. The hcp α-Mg dendrite exhibits an 18-primary-branch pattern in 3D, including the 6-primary branches along the basal directions and the other 12-primary branches along nonbasal directions. Figures 10(b)–10(i) show that as the dendrite growth proceeds,

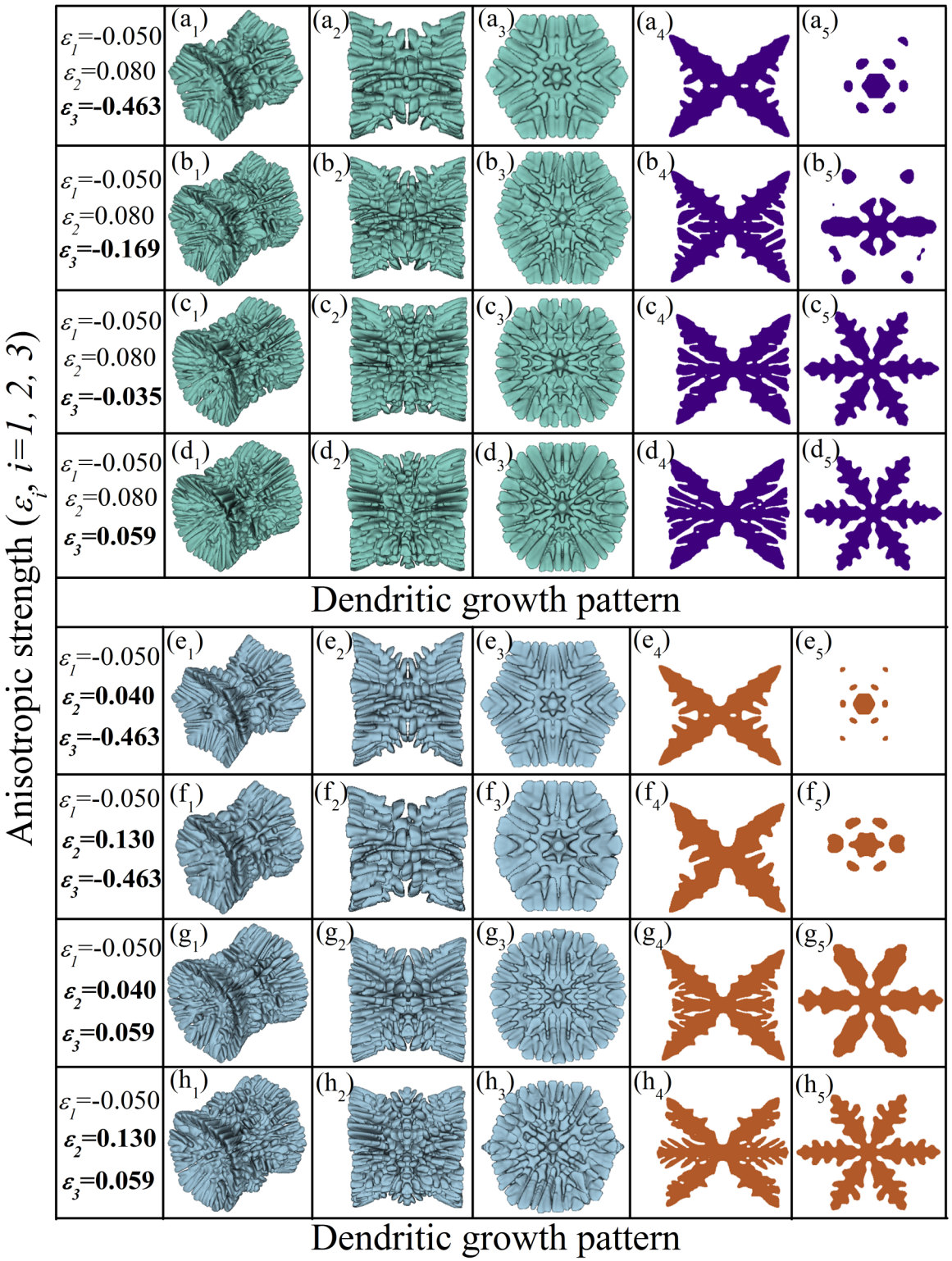

FIG. 7. Phase-field simulation on the growth pattern of the hcp α-Mg dendrite with different combinations of anisotropic strength (i.e., ε_i, $i = 1, 2, 3$).

the secondary arms exhibit the same growth direction as the dendritic primary branches. Figures 11(a)–11(c) show the according solute concentration variation at the time steps of 8000, 28 000, and 36 000, respectively. The results indicate that the solute concentration decreases as the distance from the solid/liquid interface increases, and the variation becomes larger as the supercooling increases. More solute accumulation occurs at the solid/liquid interface under a larger supercooling condition. On the other hand, when the supercooling is lower, the diffusion layer at the solid/liquid interface becomes more

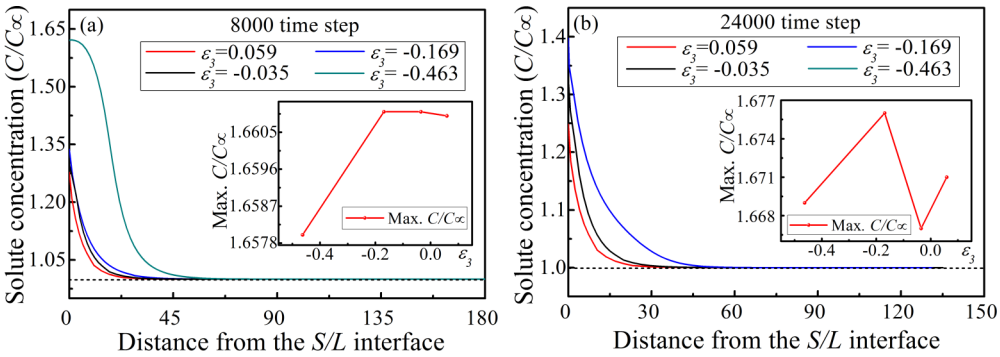

FIG. 8. Solute concentration (C/C_∞) variation versus the distance from the solid/liquid interface under different anisotropic strength ε_3 at the time steps of (a) 8000, and (b) 24 000, respectively. The inset maps show the corresponding solute concentration variation at the solid-liquid interface (i.e., the maximum solute concentration).

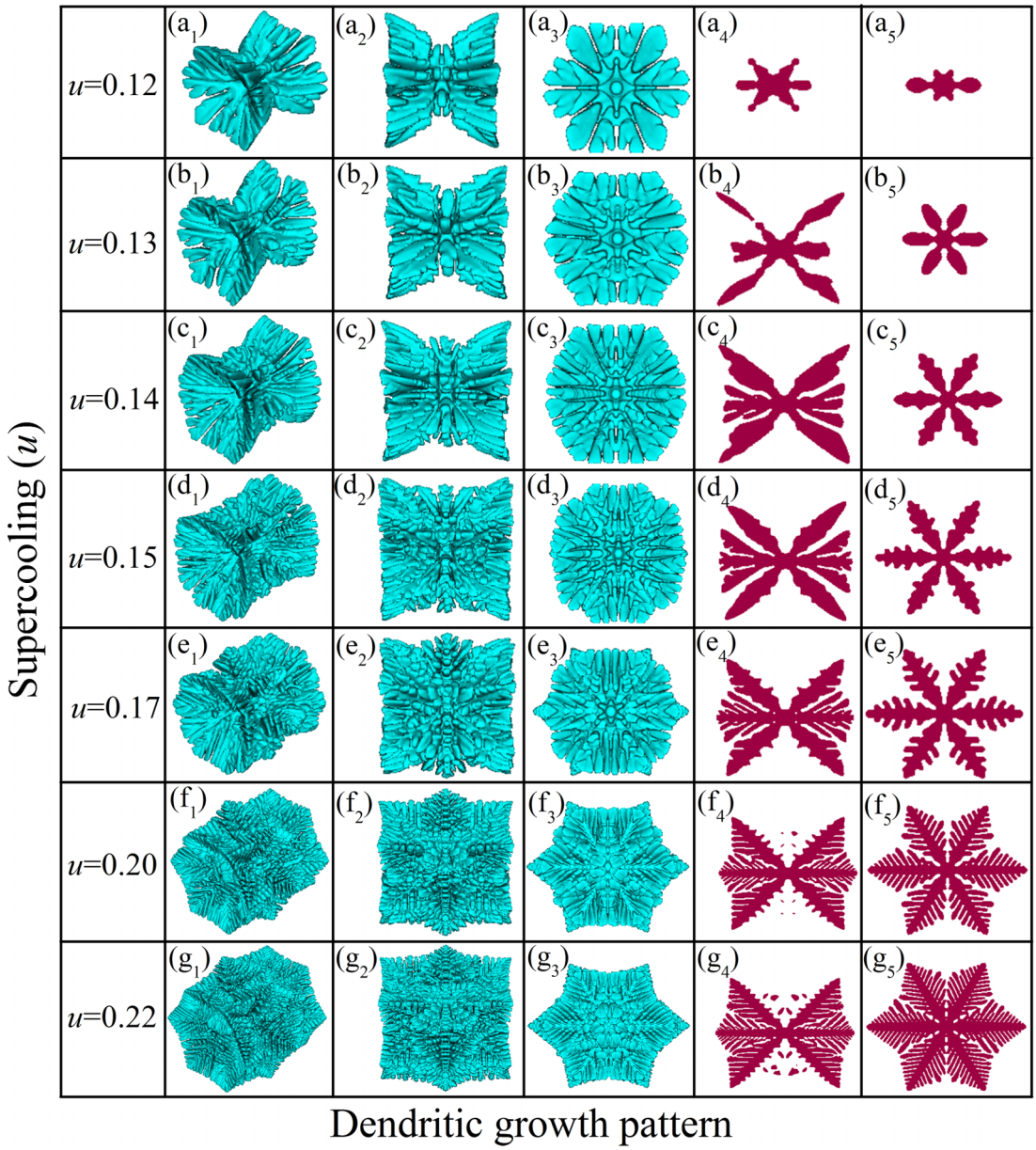

FIG. 9. Phase-field simulation on the growth pattern of the hcp α-Mg dendrite under different supercooling (u) conditions. (a_1)–(g_1) show the 3D dendritic morphology, (a_2)–(g_2) and (a_3)–(g_3) show the 2D projections of the simulated α-Mg dendrite viewed from $\langle 11\bar{2}0\rangle$ and $\langle 0001\rangle$, (a_4)–(g_4) and (a_5)–(g_5) show the according 2D sections cut by the $\{10\bar{1}0\}$ and $\{0001\}$ planes, respectively.

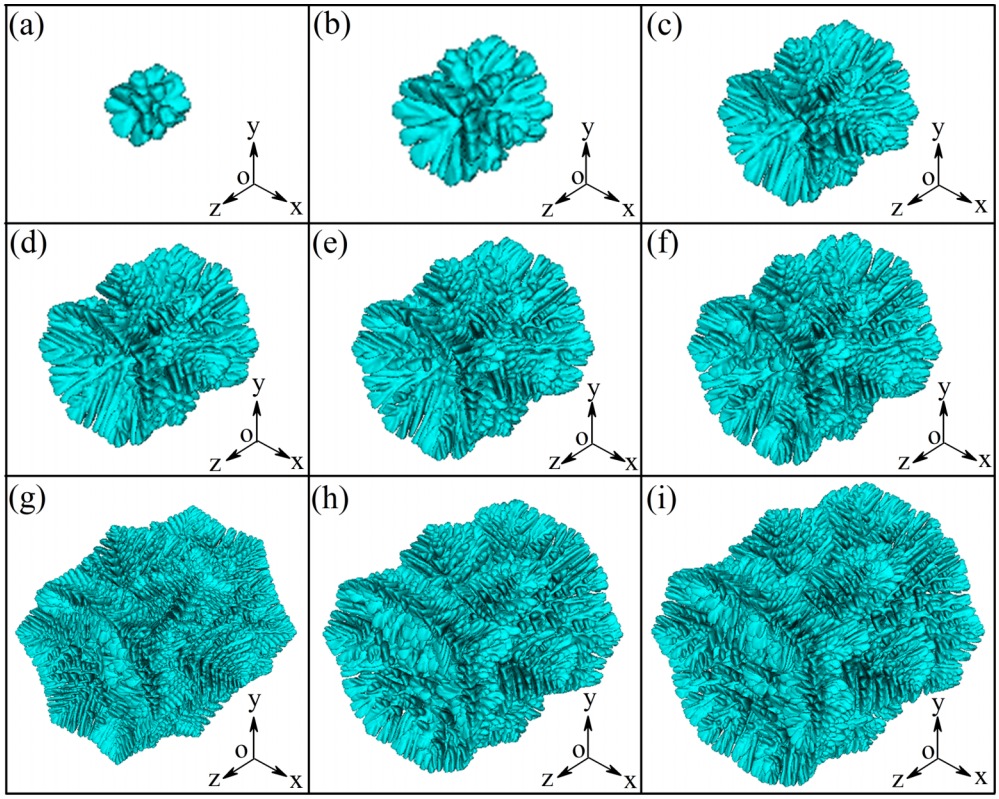

FIG. 10. Phase-field simulation on the hcp α-Mg dendrite evolution with a specific supercooling condition of $u = 0.20$ at the time steps of (a) 4000, (b) 8000, (c) 16 000, (d) 20 000, (e) 24 000, (f) 28 000, (g) 32 000, (h) 40 000, and (i) 48 000, respectively.

smeared and the solute concentration distributes more uniformly. As the solidification proceeds, the solute accumulation at the solid/liquid interface becomes more significant in the liquid region between the dendritic primary and secondary arms. Furthermore, the maximum solute concentration (i.e., at the solid/liquid interface) increases as the supercooling

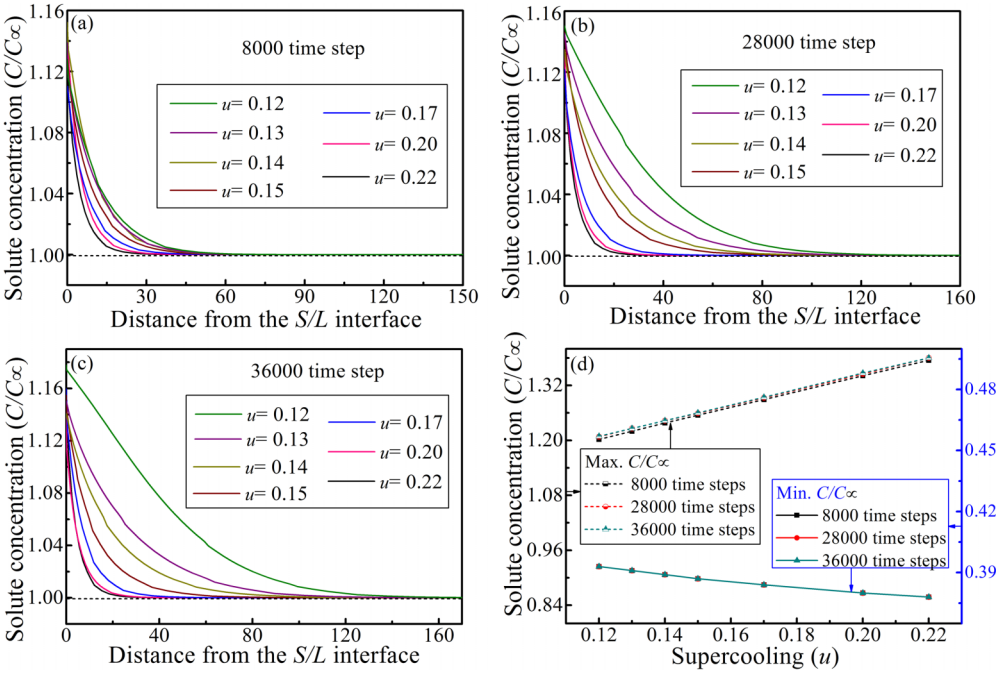

FIG. 11. Solute concentration (C/C_∞) variation versus the distance from the solid/liquid interface under different supercooling (u) conditions at the time steps of (a) 8000, (b) 28 000, and (c) 36 000. (d) shows the corresponding variation of the maximum and minimum solute concentration at different supercooling conditions.

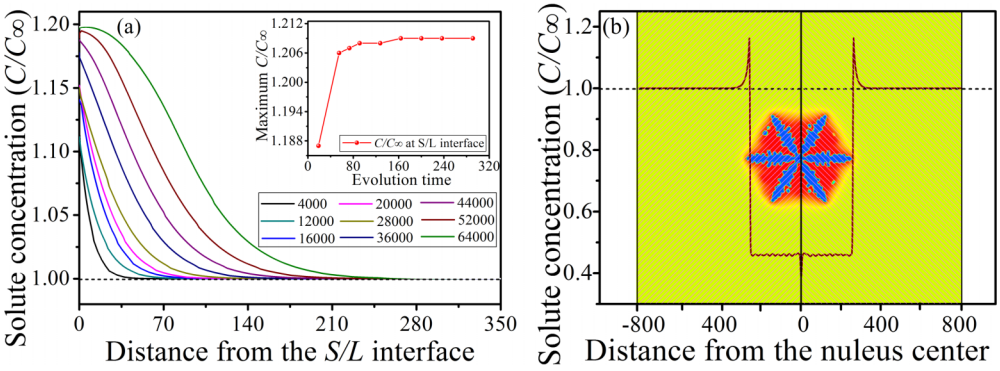

FIG. 12. (a) Solute concentration (C/C_∞) variation in the liquid close to the front of the solid/liquid interface at different time steps under a given supercooling of $u = 0.15$ and (b) solute concentration distribution at the time step of 52 000. The inset shows the solute concentration change at the solid/liquid interface (i.e., the maximum solute concentration).

increases, whereas the minimum solute concentration decreases to maintain the mass conservation, as shown in Fig. 11(d).

Figure 12(a) shows the solute concentration variation at different time steps when $k = 0.37$ and $u = 0.12$. The inset shows the corresponding variation of solute concentration at the solid/liquid interface, i.e., the maximum solute concentration. As the hcp α-Mg dendrite grows further, the variation of the solute concentration becomes insignificant, and the maximum value increases as the time evolves before reaching a constant value. Figure 12(b) shows the solute concentration distribution at the time step of 52 000. As the distance from the dendritic nucleus center increases, the solute concentration firstly achieves a local maximum at the solid/liquid interface,

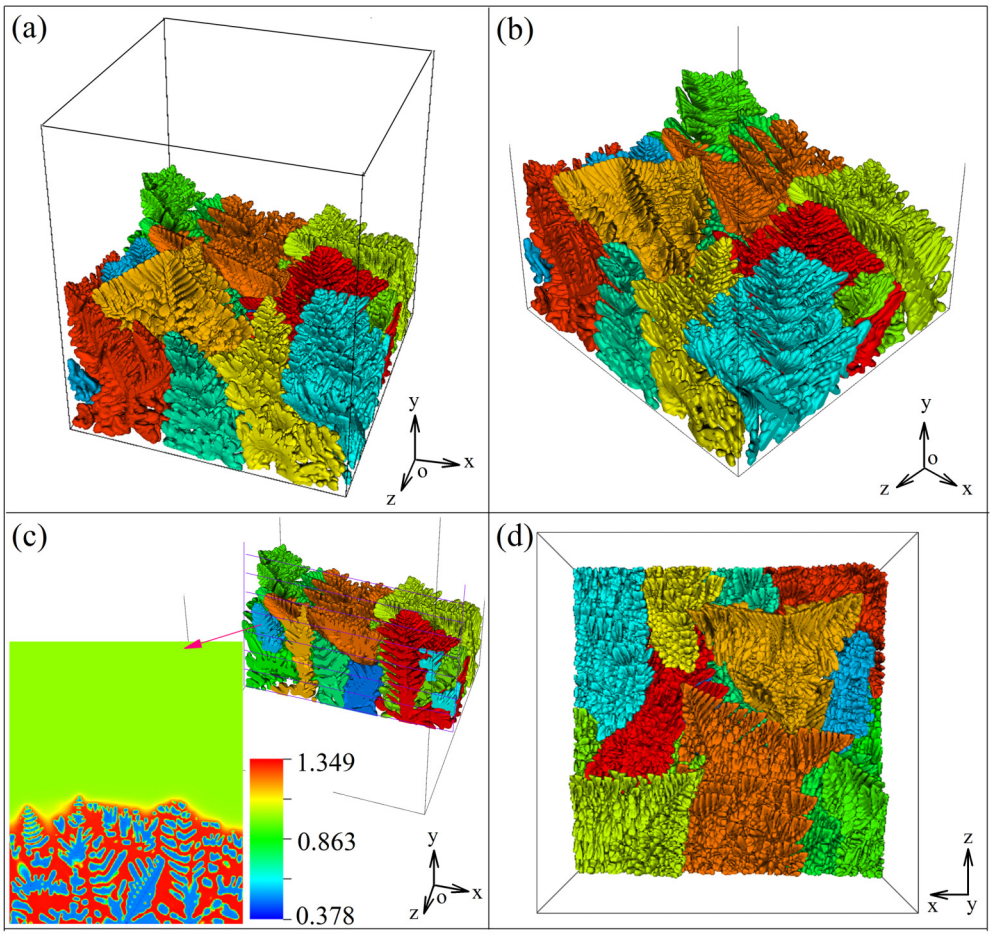

FIG. 13. 3D growth pattern of the multidendrites during directional solidification of magnesium alloy. (a) and (c) show the 3D dendritic morphology viewed from ⟨123⟩ and an according 2D solute concentration distribution of a specified section, while (b) and (d) from ⟨111⟩ and ⟨010⟩, respectively.

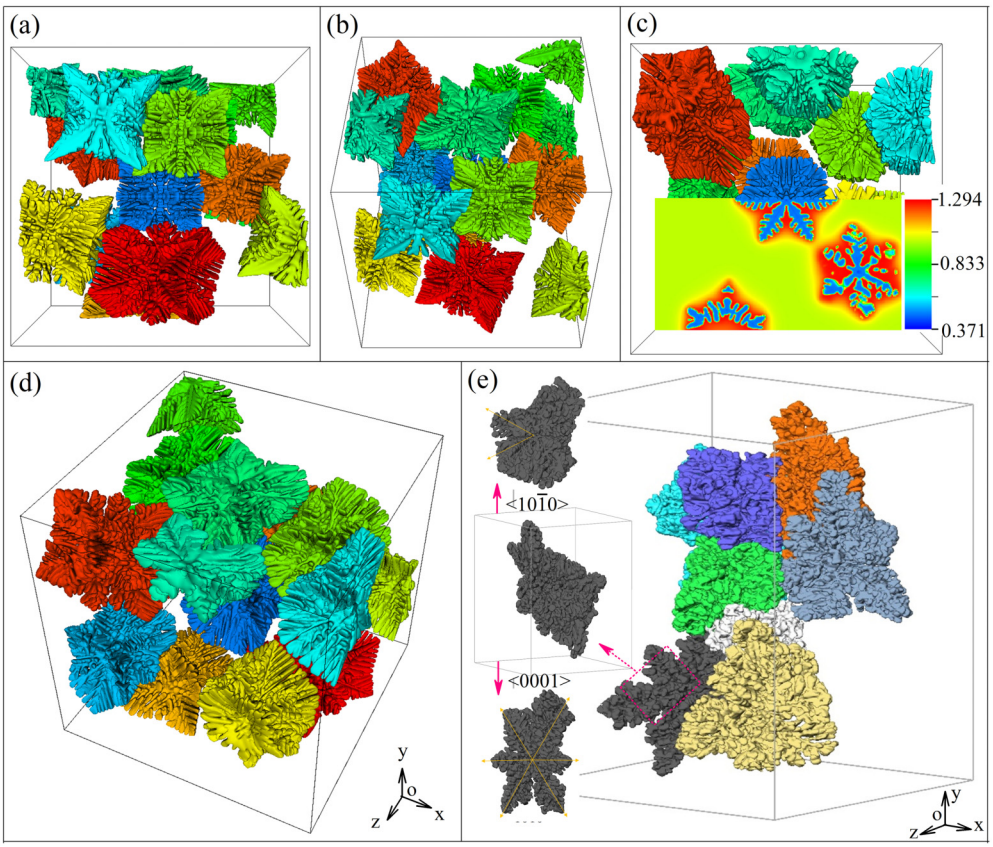

FIG. 14. 3D growth pattern of the equiaxed multidendrites of magnesium alloy viewed from different perspectives (a)–(d), compared with the 3D dendritic morphology reconstructed from synchrotron x-ray tomography experiment (e). The according solute concentration distribution of the equiaxed multidendrites is also shown in (c).

and then decreases gradually before reaching a constant value. The predicted results agree well with the existing solidification theory [63,65].

As discussed, the hcp α-Mg dendrite exhibits growth tendency along both the basal and nonbasal directions, but the dendritic growth tendency along the nonbasal directions is larger. Whether the hcp α-Mg dendrite grows along the basal directions or not is dependent on the magnitude of the local driving force, which on the other hand is associated with the growth parameters, such as the partition coefficient, the anisotropic strength, and local supercooling conditions during solidification. The consequence is that the 3D morphology of the hcp α-Mg dendrite would transform from an 18-primary-branch to a 12-primay-branch pattern [26,27]. Such growth behavior can be attributed to the difference of the dendritic growth tendency along the basal and nonbasal directions, as reflected by the surface energy anisotropy [2,28]. In particular, the basal primary branches could be inhibited by the lead growth or the overgrowth of the nonbasal ones.

E. Multidendrites growth pattern

Simulations are also performed to investigate the growth pattern formation of the columnar multidendrites of magnesium alloys formed during the directional solidification, where 15 dendritic nuclei are initialized randomly at the bottom of the computing domain. A uniform temperature gradient is then imposed along the y axis. Accordingly, the simulated results on the 3D dendritic morphology of the columnar multidendrites viewed from different perspectives are shown in Figs. 13(a), 13(b), and 13(d), respectively. A longitudinal section through the columnar multidendrites and the corresponding solute concentration distribution is also shown in Fig. 13(c). The results indicate that because of the competitive growth, some dendrites survive whereas others get blocked and disappear as the dendritic microstructure evolves. Further analysis found that the blocked dendrites are normally those with an orientation deviating from the y axis (or parallel to the temperature gradient direction). The dendritic microstructure is featured by small dendritic trunks with a sixfold symmetrical pattern and a regular arrangement of the trunks along one of these sixfold directions. The simulated dendrites are analogous with their morphology despite the growth variation of both primary and secondary arms. The results are consistent with those reported by Pettersen *et al.* [24,25].

Figure 14 shows the 3D growth pattern for equiaxed multidendrites growth of magnesium alloys. An overall 15 dendritic seeds are planted randomly within the computation domain, and all dendrites grow and impinge with each other. The simulated 3D morphology of the equiaxed multidendrites viewed from different perspectives is shown in Figs. 14(a)–14(d), respectively. The according solute concentration distribution is also presented in Fig. 14(c). It is found that the hcp α-Mg dendrites exhibit a typical sixfold symmetrical pattern in 2D due

to its hexagonal lattice structure. Each dendritic morphology exhibits an 18-primary-branch pattern in 3D, which agrees well with those found in synchrotron x-ray tomography experiments [9,12,27], as presented in Fig. 14(e). A Supplemental Material video with respect to the evolution of both equiaxed and columnar multidendrites growth of the magnesium alloy is provided in Ref. [67]. The present investigation will provide deep insight into understanding the growth pattern formation and morphological transition of the α-Mg dendrite with hcp lattice structure.

IV. CONCLUSIONS

In conclusion, the growth behavior and pattern formation of magnesium alloy dendrite are investigated, together with the discussion on the underlying mechanism behind the 3D morphological transition of the hcp α-Mg dendrite observed in experiments. The anisotropy function with the anisotropic strength quantified from DFT-based atomistic calculations is coupled into the 3D phase-field model to simulate the dendritic growth behavior. It is found that the dendritic morphological transition from the 18-primary-branch pattern to the 12-primary-branch pattern is associated with the growth parameters during solidification, including the partition coefficient, the anisotropic strength, and the supercooling conditions. The hcp α-Mg dendrite mainly exhibits growth tendency along the basal and nonbasal directions, but because of the difference in surface energy anisotropy, the dendritic growth tendency along the basal directions is lower than that along the nonbasal directions. Consequently, without enough driving force, the basal dendritic primary branches would not exhibit, as exemplified by the 3D dendritic morphology with 12-primary-branch pattern under lower supercooling condition. During solidification, the solute concentration increases from the dendritic nucleus center, and achieves the maximum at the solid/liquid interface, beyond which the solute concentration decreases before reaching a constant value.

ACKNOWLEDGMENTS

This work is financially supported by the National Key Research and Development Program of China (Grant No. 2016YFB0301001), the National Natural Science Foundation of China (Grant No. 51701104), the Postdoctoral Science Foundation of China (Grant No. 2017M610884), the Tsinghua University Initiative Scientific Research Program (Grant No. 20151080370), the Tsinghua Qingfeng Scholarship (THQF2018-15), and the UK Royal Society Newton International Fellowship Scheme. The authors acknowledge the National Laboratory for Information Science and Technology in Tsinghua University for access to supercomputing facilities.

J.D. and A.Z. contributed equally to this work.

[1] H. Hornberger, S. Virtanen, and A. R. Boccaccini, Acta Biomater. **8**, 2442 (2012).
[2] T. M. Pollock, Science **328**, 986 (2010).
[3] I. P. Jain, C. Lal, and A. Jain, Int. J. Hydrogen Energy **35**, 5133 (2010).
[4] M. Bamberger and G. Dehm, Annu. Rev. Mater. Res. **38**, 505 (2008).
[5] M. K. Kulekci, Int. J Adv. Manuf. Tech. **39**, 851 (2007).
[6] H. Hu, A. Yu, N. Li, and J. E. Allison, Mater. Manuf. Processes **18**, 687 (2003).
[7] J. Du, A. Zhang, Z. Guo, M. Yang, M. Li, and S. Xiong, Intermetallics **95**, 119 (2018).
[8] A. A. Luo, Int. Mater. Rev. **49**, 13 (2013).
[9] M. Yang, S. Xiong, and Z. Guo, Acta Mater. **92**, 8 (2015).
[10] E. Guo, A. B. Phillion, B. Cai, S. Shuai, D. Kazantsev, T. Jing, and P. D. Lee, Acta Mater. **123**, 373 (2017).
[11] S. Xiong, J. Du, Z. Guo, M. Yang, M. Wu, C. Bi, and Y. Cao, Acta Metall. Sin. **54**, 174 (2018).
[12] J. Du, Z. Guo, M. Yang, and S. Xiong, Mater. Today Commun. **13**, 155 (2017).
[13] D. Casari, W. U. Mirihanage, K. V. Falch, I. G. Ringdalen, J. Friis, R. Schmid-Fetzer, D. Zhao, Y. Li, W. H. Sillekens, and R. H. Mathiesen, Acta Mater. **116**, 177 (2016).
[14] T. Haxhimali, A. Karma, F. Gonzales, and M. Rappaz, Nat. Mater. **5**, 660 (2006).
[15] C. A. Becker, D. Olmsted, M. Asta, J. J. Hoyt, and S. M. Foiles, Phys. Rev. Lett. **98**, 125701 (2007).
[16] D. Y. Sun, M. I. Mendelev, C. A. Becker, K. Kudin, T. Haxhimali, M. Asta, J. J. Hoyt, A. Karma, and D. J. Srolovitz, Phys. Rev. B **73**, 024116 (2006).
[17] S. Shuai, E. Guo, M. Wang, M. D. Callaghan, T. Jing, Q. Zheng, and P. D. Lee, Metall. Mater. Trans. A **47**, 4368 (2016).
[18] L. Granasy, T. Pusztai, J. A. Warren, J. F. Douglas, T. Borzsonyi, and V. Ferreiro, Nat. Mater. **2**, 92 (2003).
[19] J. Hoyt, Mater. Sci. Eng., R **41**, 121 (2003).
[20] D. Danilov and B. Nestler, Phys. Rev. Lett. **93**, 215501 (2004).
[21] A. Zhang, S. Liang, Z. Guo, and S. Xiong, Exp. Therm. Fluid Sci. **88**, 472 (2017).
[22] J. Eiken, Int. J Cast Metal Res. **22**, 86 (2013).
[23] B. Böttger, J. Eiken, M. Ohno, G. Klaus, M. Fehlbier, R. Schmid-Fetzer, I. Steinbach, and A. Bührig-Polaczek, Adv. Eng. Mater. **8**, 241 (2006).
[24] K. Pettersen and N. Ryum, Metall. Trans. A **20**, 847 (1989).
[25] K. Pettersen, O. Lohne, and N. Ryum, Metall. Trans. A **21**, 221 (1990).
[26] J. Du, Z. Guo, A. Zhang, M. Yang, M. Li, and S. Xiong, Sci. Rep. **7**, 13600 (2017).
[27] M. Yang, S. Xiong, and Z. Guo, Acta Mater. **112**, 261 (2016).
[28] J. Du, Z. Guo, M. Yang, and S. Xiong, in *Proceedings of the 4th World Congress on Integrated Computational Materials Engineering (ICME 2017), Ypsilanti*, edited by P. Mason, C. R. Fisher, R. Glamm, M. V. Manuel, G. J. Schmitz, A. K. Singh, and A. Strachan (Springer, 2017), p. 263.
[29] J. Du, A. Zhang, Z. Guo, M. Yang, M. Li, and S. Xiong, ACS Omega **2**, 8803 (2017).
[30] Z. Guo, J. Mi, S. Xiong, and P. S. Grant, Metall. Mater. Trans. B **44**, 924 (2013).
[31] J. J. Hoyt, M. Asta, and A. Karma, Phys. Rev. Lett. **86**, 5530 (2001).

[32] Z. Guo, J. Mi, S. Xiong, and P. S. Grant, J. Comput. Phys. **257**, 278 (2014).
[33] Z. Guo and S. Xiong, Comput. Phys. Commun. **190**, 89 (2015).
[34] A. Zhang, Z. Guo, and S. Xiong, J. Appl. Phys. **121**, 125101 (2017).
[35] S. Sandlöbes, Z. Pei, M. Friák, L. F. Zhu, F. Wang, S. Zaefferer, D. Raabe, and J. Neugebauer, Acta Mater. **70**, 92 (2014).
[36] P. Villars and L. D. Calvert, *Pearson's Handbook: Crystallographic Data for Intermetallic Phases* (ASM International, Materials Park, OH, 1997).
[37] J. C. Mikkelsen and J. B. Boyce, Phys. Rev. Lett. **49**, 1412 (1982).
[38] P. L. Liu and Y. J. Siao, Scr. Mater. **64**, 483 (2011).
[39] J. Du, B. Wen, and R. Melnik, Comput. Mater. Sci. **95**, 451 (2014).
[40] M. C. Payne, M. P. Teter, D. C. Allan, T. A. Arias, and J. D. Joannopoulos, Rev. Mod. Phys. **64**, 1045 (1992).
[41] G. Kresse, M. Marsman, and J. Furthüller, VASP, the guide, http://cmsmpiUnivieacat/vasp/.
[42] D. Alfè and M. J. Gillan, J Phys.: Condens. Matter **18**, L435 (2006).
[43] P. E. Blöchl, Phys. Rev. B **50**, 17953 (1994).
[44] A. Fitzgibbon and M. Pilu, IEEE Trans. Pattern Anal. Mach. Intell. **21**, 476 (1999).
[45] J. M. Lee, K. K. Jung, and J. S. Ko, J. Electrochem. Soc. **163**, D407 (2016).
[46] E. Asadi and M. Asle Zaeem, Acta Mater. **107**, 337 (2016).
[47] B. Echebarria, R. Folch, A. Karma, and M. Plapp, Phys. Rev. E **70**, 061604 (2004).
[48] T. Takaki, ISIJ Int. **54**, 437 (2014).
[49] N. Eustathopoulos, Int. Metal. Rev. **28**, 189 (1983).
[50] J. V. D. Planken and A. Deruyttere, J Cryst. Growth **11**, 273 (1971)
[51] D. Sun, M. Zhu, J. Wang, and B. Sun, Int. J. Heat Mass Transf. **94**, 474 (2016).
[52] L. Gránásy, T. Pusztai, T. Börzsönyi, J. A. Warren, and J. F. Douglas, Nat. Mater. **3**, 645 (2004).
[53] M. Amoorezaei, S. Gurevich, and N. Provatas, Acta Mater. **60**, 657 (2012).
[54] N. A. Ahmad, A. A. Wheeler, W. J. Boettinger, and G. B. McFadden, Phys. Rev. E **58**, 3436 (1998).
[55] W. Kurz, B. Giovanola, and R. Trivedi, Acta Metall. **34**, 823 (1986).
[56] A. Zhang, Z. Guo, and S. Xiong, China Foundry **14**, 373 (2017).
[57] A. Zhang, Z. Guo, and S. M. Xiong, Phys. Rev. E **97**, 053302 (2018).
[58] A. A. Wheeler, W. J. Boettinger, and G. B. McFadden, Phys. Rev. E **47**, 1893 (1993).
[59] Y. T. Zhang, Y. Chi, and C. Q. Hu, China Foundry **14**, 184 (2017).
[60] V. G. Smith, W. A. Tiller, and J. W. Rutter, Can. J. Phys. **33**, 723 (1955).
[61] W. A. Miller and G. A. Chadwick, Proc. R. Soc. A **312**, 257 (1969).
[62] G. A. Chadwick and W. A. Miller, Met. Sci. J. **1**, 132 (1967).
[63] W. A. Tiller, K. A. Jackson, J. W. Rutter, and B. Chalmers, Acta Metall. **1**, 428 (1953).
[64] P. Hartman and W. G. Perdok, Acta Crystallogr. **8**, 49 (1955).
[65] S. Kobayashi, Trans. ISIJ **28**, 535 (1988).
[66] M. Asta, C. Beckermann, A. Karma, W. Kurz, R. Napolitano, M. Plapp, G. Purdy, M. Rappaz, and R. Trivedi, Acta Mater. **57**, 941 (2009).
[67] See Supplemental Material at http://link.aps.org/supplemental/10.1103/PhysRevMaterials.2.083402 for the video related to the evolution of equiaxed and columnar multidendrites growth of the magnesium alloy.